*Geophysical Research Letters*

Supporting Information for

# Supererruptions in Northwestern Arabia Terra reveal an early stage of Mars' mantle evolution

Augustus Bates[1]*, S. Goossens[2], J. M. Lorenzo[1], L. Ojha[3], D. R. Hood[4], S. Karunatillake[1], S. Kobs Nawotniak[5], T. Paladino[5]

[1]Department of Geology and Geophysics, Louisiana State University, Baton Rouge, LA, USA

[2] NASA Goddard Space Flight Center

[3]Rutgers, The State University of New Jersey

[4]Baylor University

[5]Idaho State University

## Contents of this file

Text S1 to S3
Figures S1 to S3
Table S1

## Introduction

The following descriptions are available for contextual purposes: region selection justification (text S1), numerical age estimates and compositional analyses methodology details (text S2), and the details of the geophysical modeling detailed methodology (text S3). Each of these sections provides additional details on the methods used to generate the data for the figures presented in the main text as well as the corresponding figures in the supplement.

**Text S1. Numerical age estimates and compositional analyses methodology**

*Numerical age estimates*

The Northwest region of Arabia Terra represents one of the oldest terrains on Mars, resulting in geologic heterogeneity that could bias geochemical trends if regional investigations disregard geologic units. Therefore, we examine two regions, the volcanic Super-eruption Context Region (SCR) and Broad-SCR, following mapped geology (K.L. Tanaka et al., 2014), regional geochemistry (Taylor et al., 2010), and topography (Carnes et al., 2017). The Broad-SCR region encloses the smaller SCR region, making chemical comparisons between the two useful for characterizing the distinctness of the chemistry found within SCR. Using our prior delineations (Carnes et al., 2017), we calculated a crater-based age for both Arabia regions. We use two complementary methods for the purpose: 1) crater-based numerical average (Fig. S1B), calculated using CratercountsII software (Arvidson et al., 1979; Hartmann et al., 2001; Werner & Tanaka, 2011) and 2) mapped geology based categorical age distribution (Fig. S1A) (K.L. Tanaka et al., 2014). Our crater-based age was derived using the CratercountsII software in conjunction with ArcGIS. We manually map craters by defining the rim of a crater with 3 points, to which a circle was then fit. We then used our manually mapped craters to calculate an age using CraterstatsII, with a diameter cutoff of 16 km, which gives a more precise age fit to the geochrons (Hartmann et al., 2001; Werner & Tanaka, 2011). Both methods allowed us to validate our age analyses over the areas, as crater-based dating methods become increasingly biased as area decreases, while mapped geology primarily yields a categorical relative age (Arvidson et al., 1979).

*Compositional analyses*

The GRS-derived gamma spectra archived at the PDS are the source of our chemical maps, as also used in prior works (Baratoux et al., 2011; Don R. Hood et al., 2019; Donald R. Hood et al., 2016; Ojha et al., 2019; Parro et al., 2017; Susko et al., 2017). The derivation follows the published spectra-to-chemistry modeling methods (Boynton et al., 2007; Evans et al., 2006; Karunatillake et al., 2007). Due to the nature of the derivation methods (e.g., elements like Fe and Si, with abundances determined from scatter and capture nuclear reactions induced by the galactic cosmic fluxes), the chemical maps are generally restricted to the mid-to-low latitudes where H abundances are sufficiently low. Likewise, GRS data provide the chemistry for nine major elements to decimeter depths below the martian surface, likely deeper than the surface dust cover (Ruff & Christensen, 2002) for the martian midlatitudes. The percentage mass fraction (wt%) of the elements discussed in this study, including Si, Ca, and stoichiometric $H_2O$, are binned into 5° × 5° pixels primarily across the mid-to-low latitudes (roughly 60° to -60°).

Given the insight from the four elements (chemical and geophysical trends section in the manuscript), we compare K, Th, S and Cl from notable Noachian volcanic regions (i.e., Thaumasia Planum, Hesperia Planum and Apollinaris Mons) as well as Argyre, Hellas, Isidis and Eridania sedimentary regions to assess the inter- and intra-regional chemical

trends in igneous and sedimentary settings. We notably exclude $H_2O$ analyses, due to the difficulties in attributing any $H_2O$ abundance trends to a particular process. That is primarily a result of $H_2O$'s varying phases and chemical affinities through different timescales as well as latitudinal dependence of abundance on the martian surface (Clifford et al., 2010; Feldman et al., 2004). In addition, mineral abundance alone cannot account for all measured $H_2O$ (Fialips et al., 2005), making it difficult to attribute a measured $H_2O$ abundance to a specific process or the prevalence of a given mineral group.

The data for each sedimentary and volcanic region are extracted as pixels from the chemical maps with centroid latitude and longitude that falls within each delineated area. For context on a chemical signature from volcanic eruptions in SCR, we examine S and Cl trends in bivariate space across the aforementioned regions, along with reported mean values of S and Cl from the MFF given its possibly pyroclastic origin (Ojha et al., 2018). We analyze K and Th similarly, particularly relative to the linear global trend between the two elements (Taylor et al., 2006). From that, relative enrichments in K and Th become evident between our selected regions and their degree of divergence from the linear trend provides insight into possible alteration processes. We compare these results with the rest of the GRS dataset, as a proxy for the average composition of the martian crust (Karunatillake et al., 2011). We report errors of the average abundances of K, Th, S and Cl. We estimate K/Th uncertainty as $(K/Th)[(\sigma_K/K)^2+(\sigma_{Th}/Th)^2]^{1/2}$, where K and Th are the mean concentration of K, Th (Taylor et al., 2006). The same method is used for S/Cl, where abundances of K and Th are substituted for S and Cl, respectively. Sigma is the propagated numerical uncertainty associated with the mean values of the elements in question.

The crustal reference in Fig. S2 reveals several key trends. The Si content in SCR is slightly enriched compared to the martian crust, consistent with sourcing from a dry, depleted mantle during the transition from Noachian to Hesperian (Balta & McSween, 2013). Ca shows a much higher degree of enrichment, also consistent with a mantle source during this same transition, as there is a shift to more high-Ca pyroxene content over low-Ca at the Noachian/Hesperian boundary (Baratoux et al., 2013). $H_2O$ enrichment can be attributed to efficient scavenging of water – possibly as nucleated ice -- from the martian atmosphere via pyroclasts (Wilson & Head, 2007), if we discount the temporal instability of water on Mars. Furthermore, density estimates are consistent with ice-rich material (Ojha & Lewis, 2018), where ice may sublimate post-deposition creating fretted terrains, a common feature within Arabia and SCR (Denton & Head, 2019).

**Text S2. Region Selection**

Based on the derived SCR age, we identify three contemporaneous Noachian volcanic provinces as type references for compositional comparisons: Thaumasia Planum, Hesperia Planum, and Apollinaris Mons. These igneous references were chosen based on age overlap with SCR and areal extent. Sufficient spatial scale is necessary when using GRS data as sampling bias becomes more prominent when area decreases. This is primarily a function of GRS's coarse resolution (450 km/pixel; Hood et al., 2016); it is most useful for investigating regional trends, not at the scale of individual craters or paterae. Our three igneous references also cover a wide range of eruptive styles, as Apollinaris is inferred to have erupted explosively in its past (Kerber & Head, 2010). Hesperia and Thaumasia are large igneous provinces that were active during the Late Noachian and Early Hesperian, which may contain compositional trends of magma across this boundary in time.

We also selected several sedimentary references (Isidis, Hellas, Argyre and Eridania) that have similar ages as SCR. Among the references, we regard Isidis' chemistry to represent igneous processes as its Middle Noachian (Ehlmann et al., 2011) formation includes extensive volcanic resurfacing from impact induced magmatism. This resulted in two distinct olivine-rich layers that are km-scale in thickness (Hamilton et al., 2003; Mustard et al., 2009). While there is substantial geomorphological evidence for abundant fluvial activity around and within Isidis, much of it dissipated post-impact (Mustard et al., 2009). Had fluvial activity persisted after the Isidis olivine-rich layer formed, pervasive alteration would have resulted because olivine alters readily, but there is little evidence for such large scale alteration (Mustard et al., 2009). The olivine layer has also been hypothesized to underlie material within the Isidis basin, and extend laterally outward (Boyce et al., 2006). Since the olivine unit is the dominant underlying bedrock layer, the regolith was likely derived primarily from mechanical erosion of the olivine layer with minimal chemical weathering (Newsom et al., 2007). That scenario would result in an overall igneous chemistry at the scale of our chemical maps. Furthermore, Syrtis Major's eruptions could have deposited fine grained volcaniclastic material within the low topography of Isidis (Kerber et al., 2012), particularly given spatial proximity.

We regard Hellas as a reference for low-pH alteration of mafic chemistry. Hellas is hypothesized to have been formed by an impact somewhat earlier and more energetic than Isidis (Ehlmann et al., 2011), which resulted in magmatism around the basin. This magmatism created volcanic edifices surrounding the basin rim, which deposited volcanic units within the basin itself. Hellas is an area of extremely low topography and surrounding volcanics, all of which have contributed basin sediment (Moore & Edgett, 1993; Salese et al., 2016; Kenneth L. Tanaka, 2002). However, prior work has interpreted chemical data within Hellas as evidence for regional low-pH alteration within the basin (Zalewska, 2013) which is corroborated by the numerous valley networks along Hellas' rim (Grau Galofre et al., 2020). These valley networks were likely contemporaneous with the surrounding volcanics or post-date them, as fluvial activity peaked in the Hesperian (Grau Galofre et al., 2020). Therefore, it is likely that the chemistry of the basin floor is

heavily altered and would best described as aqueous alteration of basalt and sulfate formation through evaporation of water (Zalewska, 2013).

We chose a sedimentary reference to the east of Hellas, which we call Eridania for brevity, comprised of highland geologic units that show evidence of heavy fluvial erosion and feature a variety of depositional processes ranging from eolian and fluvial to ash fall (Mest & Crown, 2014; K.L. Tanaka et al., 2014). Our delineation of this region differs from prior works (Michalski et al., 2017), as we focus on portions of this area that are sedimentary in origin and have been heavily weathered (Mest & Crown, 2014; K.L. Tanaka et al., 2014). Eridania, which contains parts of Promethei Terra and Eridania Planitia, is comprised of 2 generalized units: a Hesperian and Noachian undivided unit and a Noachian highland undivided unit (K.L. Tanaka et al., 2014). The former is described as friable, likely containing sedimentary, volcanic and impact rocks and has been altered by weathering. The latter is more representative of occasional tectonic contraction (K.L. Tanaka et al., 2014). A more descriptive geologic analysis of the western portion of the area suggests deposition under lacustrine settings (Mest & Crown, 2014). Therefore, for this study, Eridania represents a mixture of material from a variety of depositional mechanisms that has been heavily altered by weathering.

For our final sedimentary reference, we selected Argyre as it is another impact-formed depositional basin. Prior works have also shown that it lacks convincing proximal or interior volcanics, implying deposition through secondary processes (Kerber et al., 2012). The Argyre deposits show evidence of heavy erosion, primarily by eolian processes with some modification through glacial activity (Kerber et al., 2012), and are hypothesized to be derived from fluvial and glacial activity throughout its early evolution (Dohm et al., 2015). Therefore, Argyre exemplifies bulk regolith sedimentary fill as thoroughly mixed eolian material weathered in the presence of liquid or frozen water, and secondary influences from volcanism (Dohm et al., 2015; Kerber et al., 2012).

For further insight into S and Cl trends on Mars and within SCR, we also chose the Medusae Fossae Formation (MFF) as a reference. The MFF is one of the largest friable deposits on Mars (Diez et al., 2009; Ojha et al., 2018), and holds the highest observed S and Cl abundances on the martian surface (Ojha et al., 2019). This reference is key to distinguish the provenance of SCR's observed S and Cl abundances, and, in particular, to determine if the observed S and Cl values are consistent with volcanic degassing, similar to what is proposed for the MFF (Diez et al., 2009).

To minimize overlap bias, we exclude SCR and BSCR from the bulk crustal proxy constituted of the entire mid-to-low latitudinal areas. In the ensuing analyses, we examine the geochemical consistency between SCR and the reference region types: volcanic, sedimentary basins, and impact-induced magmatism to investigate the provenance of SCR's chemistry.

**Text S3. Geophysical modeling methodology**

For our geophysical estimations, we use topographic data from the Mars Orbiter Laser Altimeter (MOLA), archived at NASA PDS, and used in the MarsTopo2600 model (M. A. Wieczorek, 2015). The gravity model used in our analysis is at the NASA Goddard Space Flight Center's Planetary Geodynamics Data Archive. From these data, we analyze the admittance between gravity and topography to determine parameters related to the structure of the crust and the loads on the crust used in the modeling. The admittance can be expressed as the transfer function between topography and gravity and contains important information about the structure and processes in the crust. It is defined as the cross-power of the functions divided by the power of topography (M. A. Wieczorek, 2015). When both are expressed in spherical harmonics of degree $n$ and order $m$, and the cross-power is defined as $S_{gt}(n) = \sum_{m=-n}^{m=n} g_{nm} t_{nm}$ , where $g_{nm}$ and $t_{nm}$ are the spherical harmonics coefficients of gravity $g$ and topography $t$, respectively, the admittance $Z(n)$ is then expressed as $Z(n) = S_{gt}(n)/S_{tt}(n)$. In addition, correlations per degree $n$ are defined as: $\gamma(n)=Sgt(n)/sqrt(S_{gg}(n)S_{tt}(n))$.

For our geophysical analysis, we used a localized spectral approach (Mark A. Wieczorek & Simons, 2005, 2007) to compute localized admittance and correlations. Our spherical cap has a radius of 15˚ and is centered on -5˚E, 25˚N (Fig. S3, Table S1). We use one taper with a bandwidth of $L_{win}$=30 such that the concentration of the taper is 99.99%. We use the degree and order 150 expansion of Mars' gravity field, which was specifically derived to maintain high correlations with topography, while the power in the model was still fully determined by the data (Goossens et al., 2017), and the MarsTopo2600 model for topography (M. A. Wieczorek, 2015), which is based on Mars Orbiter Laser Altimeter (MOLA) data (Smith et al., 2001). While in general a multi-taper approach is preferred to reduce the errors in the estimated spectra (Mark A. Wieczorek & Simons, 2005), the current resolution of the models does not allow such an analysis.

To prepare the measured admittance and correlations from the topography and gravity field models, we downward continue the gravity field model to the average radius in the area of interest (~3390 km) and then compute the localized admittance and correlation. We then compute theoretical admittance models and compare them to the measured admittance. For the theoretical models, we use the formulation and model of admittance from a prior work (Grott & Wieczorek, 2012) to conduct our analyses. We use both top (or surface) and bottom (or subsurface) loading in our admittance model, and they are assumed to be in phase, and thus correlations between gravity and topography should be unity. In future work, fitting admittance and correlation separately could be considered. Under the assumption that correlations less than unity are due to unmodeled gravitational signals that are uncorrelated with topography, the variance of the admittance is directly related to the correlation per spherical harmonic degree (M. A. Wieczorek, 2015; Mark A. Wieczorek, 2008). For correlations larger than 0.8, the signal-to-noise is 1.78, and we find correlations > 0.8 for spherical harmonics degrees > 77 for our chosen localization.

We thus use the degree range 77-120 to fit theoretical admittance models that depend on the following parameters: crustal density, load density, crustal thickness, elastic

thickness, load depth, and load ratio. The load ratio $L$ is defined such that it varies between -1 and (see Grott & Wieczorek, 2012), with $L > 0$ corresponding to subsurface and surface loads of the same sign, and $L < 0$ to those of opposite sign. Because we use the degree and order 150 expansion for the gravity field model as presented by Goossens et al. (2017), we can use degree 120 as the upper limit, since the upper limit is determined from $L_{max}$-$L_{win}$ (Mark A. Wieczorek & Simons, 2005, 2007). Correlations for this model are still sufficiently high as stated above (see also Fig. 4A and S4) and this allows us to increase the degree range over which to fit the theoretical model, compared to using a degree and order 120 expansion which would only allow the range 77-90.

We apply a straightforward grid search to find the best-fit admittance models in the 77-120 degree range, by computing the theoretical admittance for each parameter combination, and applying the same downward continuation and localization as we applied to the measured admittance. The grid bounds for our search are given in Table S1. Using those bounds and step size (Table S1), we evaluate roughly 40 million models. For each model, we compute the root-mean-square (RMS) of the difference between theoretical and measured admittance over the degree range 77-120.

Next, from the 40 million models, we select only those that fit the admittance within twice the best-fit RMS (which is the lowest RMS we find in the entire set). That results in a sub-selection of eventually only 71 models. We investigate the spread in the parameter values from the sub-selection to establish which parameters can be constrained, keeping in mind that while our search space was large, the sub-selection is only a tiny part of this. A more directed search or finer step-sizes around the best-fit parameters would increase the number but we do not expect that the overall picture would change much.

We find that the best-constrained parameters are the load density and elastic thickness. We define "best-constrained" as those parameters from the best-fit collection for which the histograms of their spread show some concentration around certain values, as opposed to parameters that show a flat histogram that spans their entire range. Based on the spread in the estimated values, load density and elastic thickness show the most reasonably clustered histograms. Other parameters were estimated, but ensuing histograms were inconclusive in terms of an overall trend towards either low or high values. The load ratio is also reasonably constrained, and we specifically find that the inclusion of bottom loading improves the fit greatly: a top-loading model without bottom loading cannot map the admittance signal and results in a much higher RMS of fit. We did model this region with a top-only loading model, but it failed to capture the entirety of the admittance signal. Thus, we employed a mixed loading model which was better suited to capturing the entire admittance signal. The crustal density, crustal thickness and load depth show a large spread and cannot be determined robustly. This work thus considers only these two parameters in its discussion of SCR's provenance. In summary, only models with mixed bottom and top loading, low elastic thickness and a load density of ~1500 kg/m$^3$ were suitable to account for the observed admittance signal. This motivates future work which considers simultaneous fitting of admittance and correlation, using loads that are out of phase, for additional insight into the unusual crust-mantle boundary conditions within NW Arabia during Noachian Mars.

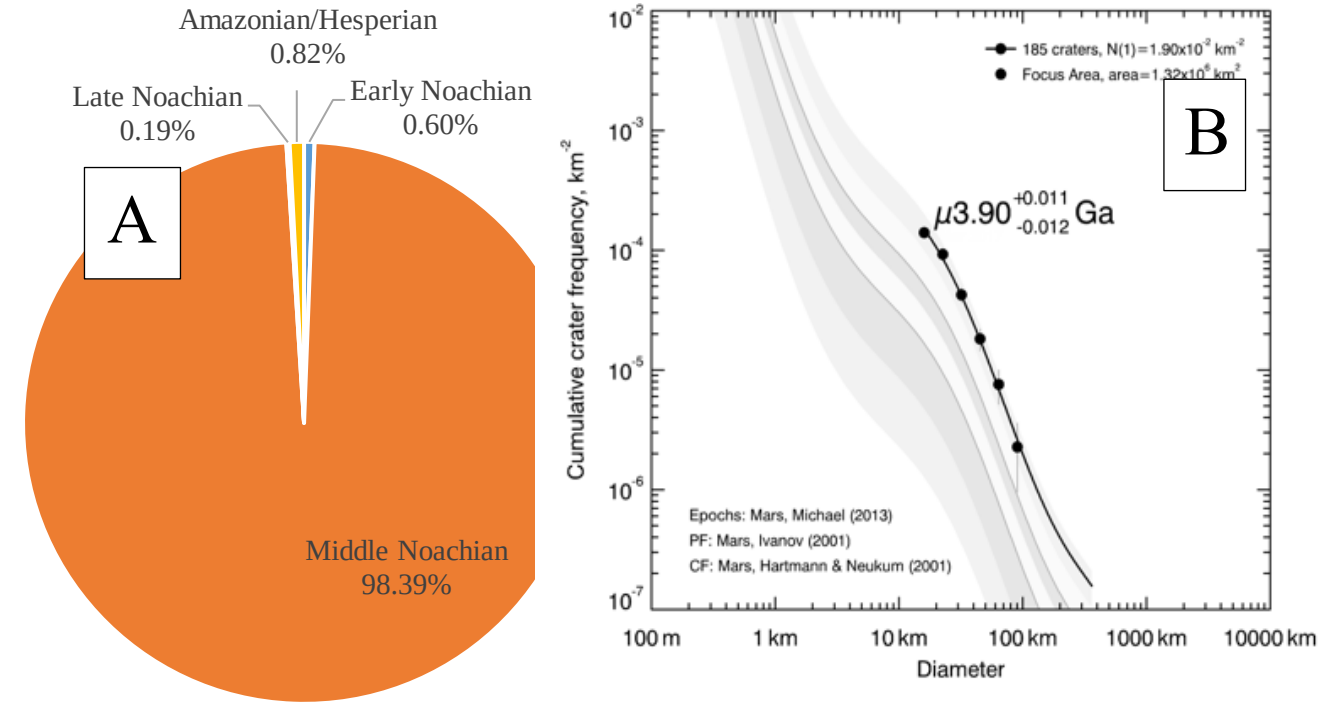


**Figure S1, (A)**: Pie chart showing the areal distribution of geologic age categories for SCR, using mapped geology (CITATION FORMAT! 1). The predominant geologic age is Middle Noachian which constitutes ~98% of the area in SCR. The remaining ~2% of terrain mostly corresponds to younger eon(s). The chart primarily describes the landscape age distribution, so it effectively characterizes the age of material analyzed through chemical maps. **(B)**: Crater-counting derived average numeric age for SCR. The calculated age from crater counting corresponds to the Middle Noachian (3.8 -3.9 Ga), which agrees with mapped-geology of (A). The spectrum of gray bands (Fig S1, B) is the martian chronostratigraphic age divisions, which are used to determine numerical age from crater data.

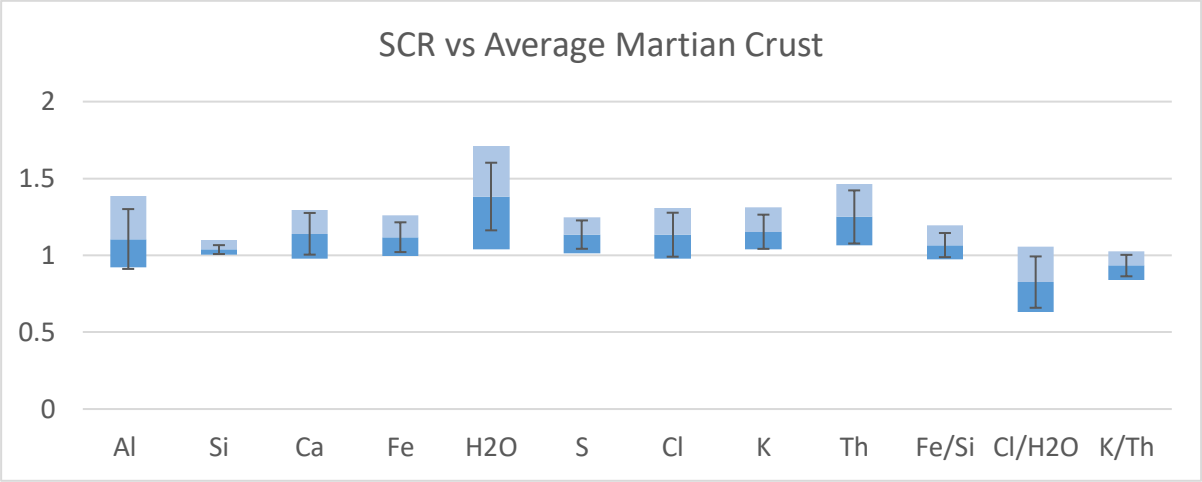


**Figure S2:** All elements measured by GRS within SCR compared to the average martian crust. The average crust is all the data from the GRS instrument, with SCR removed, thus providing a comparison between SCR and the rest of the dataset. This plot shows SCR compared to the Martian crust. Boxes are bound by ratio of $75^{th}/25^{th}$ %-ile, $50^{th}/50^{th}$, $25^{th}/75^{th}$ to visually summarize the distributional comparison for any given element between two areas. Where the $50^{th}/50^{th}$ %-ile lies on y=1, the median value of that element is the same between both regions. Error bars are propagated ratios of the median absolute deviations, capturing the deviation of values from the corresponding medians. SCR is enriched in every analyzed element compared to the crust, with notable enrichments in Si, Ca and $H_2O$.

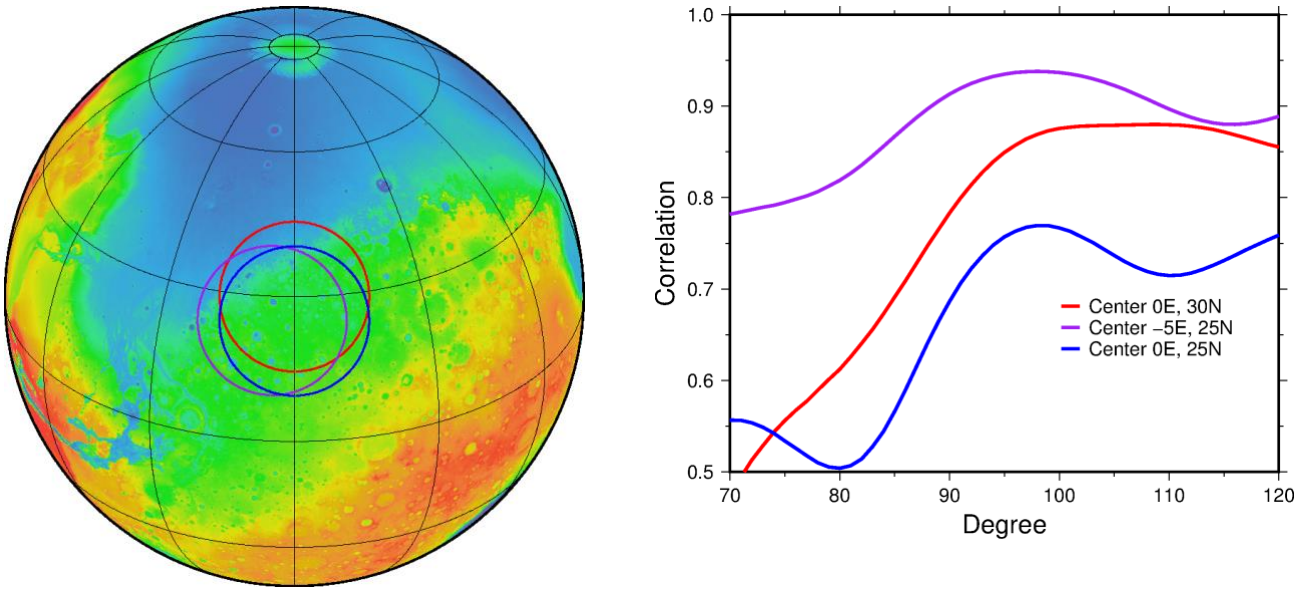


**Figure S3**: We considered several different localization windows, both in a search for a sufficient correlation between topography and gravity and a radius that accurately encompassed SCR. The purple circle reflects the most geographically accurate outline for SCR, and also shows the highest correlation (> 0.8) across the window. Other windows (red, blue) showed sufficient correlations, suggesting that our final window selection is not an outlier in comparison to other windows within Arabia. The purple localization was then used to estimate geophysical parameters, which are summarized in Table S2. High correlations between gravity and topography are preferred: results follow for center at -5˚E, 25˚N (purple), but there are relatively high correlations for regions in the immediate vicinity of the SCR.

**Table S1:** A list of the parameters that are varied in our grid search for a best fit theoretical admittance model, including the range applied and the step size taken.

| Parameter [unit] | Range | Step size |
|---|---|---|
| **Crustal thickness [km]** | 5-100 | 5 |
| **Elastic thickness [km]** | 5-150 | 5 |
| **Crustal density [kg/m$^3$]** | 2400-3100 | 50 |
| **Load density [kg/m$^3$]** | 1600-2500 | 50 |
| **Load depth [km]** | 5 - 100 | 10 |
| **Load ratio [no unit]** | -0.95-0.95 | 0.1 |
| **Note: load depth cannot exceed crustal thickness** | | |

## References


Arvidson, R. E., Boyce, J., Chapman, C., Cintala, M., Fulchignoni, M., Moore, H., et al. (1979). Standard Techniques for Presentation and Analysis of Crater Size-Frequency Data. *Icarus*, *474*, 467–474. https://doi.org/10.1016/0019-1035(79)90009-5

Balta, J. B., & McSween, H. Y. (2013). Water and the composition of Martian magmas. *Geology*, *41*(July), 1115–1118. https://doi.org/10.1130/G34714.1

Baratoux, D., Toplis, M. J., Monnereau, M., & Gasnault, O. (2011). Thermal history of Mars inferred from orbital geochemistry of volcanic provinces. *Nature*, *472*(7343), 338–41. https://doi.org/10.1038/nature09903

Baratoux, D., Toplis, M. J., Monnereau, M., & Sautter, V. (2013). The petrological expression of early Mars volcanism. *Journal of Geophysical Research E: Planets*, *118*(1), 59–64. https://doi.org/10.1029/2012JE004234

Boyce, J. M., Mouginis-Mark, P., Garbeil, H., & Tornabene, L. L. (2006). Deep impact craters in the Isidis and southwestern Utopia Planitia regions of Mars: High target material strength as a possible cause. *Geophysical Research Letters*, *33*(6), 2–5. https://doi.org/10.1029/2005GL024462

Boynton, W. V., Taylor, G. J., Evans, L. G., Reedy, R. C., Starr, R., Janes, D. M., et al. (2007). Concentration of H, Si, Cl, K, Fe, and Th in the low- and mid-latitude regions of Mars. *Journal of Geophysical Research*, *112*, E12S99. https://doi.org/10.1029/2007JE002887

Carnes, L. L., Karunatillake, S., Susko, D. A., & Hood, D. R. (2017). Delineating the Arabia Terra region on Mars to investigate paterae orgins. In *LPSC2017* (p. Abstract 1756). https://doi.org/10.1038/ngeo2845

Clifford, S. M., Lasue, J., Heggy, E., Boisson, J., McGovern, P., & Max, M. D. (2010). Depth of the Martian cryosphere: Revised estimates and implications for the existence and detection of subpermafrost groundwater. *Journal of Geophysical Research*, *115*(E7), 1–17. https://doi.org/10.1029/2009je003462

Denton, A., & Head, J. W. (2019). FRETTED CHANNELS AND CLOSED DEPRESSIONS IN NORTHERN ARABIA TERRA, MARS: ORIGINS AND IMPLICATIONS FOR SUBSURFACE HYDROLOGIC ACTIVITY. *LPSC 2019 Abstract*, (1082), 10–11.

Diez, B., Feldman, W. C., Mangold, N., Baratoux, D., Maurice, S., Gasnault, O., et al. (2009). Contribution of Mars Odyssey GRS at Central Elysium Planitia. *Icarus*, *200*(1), 19–29. https://doi.org/10.1016/j.icarus.2008.11.011

Dohm, J. M., Hare, T. M., Robbins, S. J., Williams, J. P., Soare, R. J., El-Maarry, M. R., et al. (2015). Geological and hydrological histories of the Argyre province, Mars. *Icarus*, *253*, 66–98. https://doi.org/10.1016/j.icarus.2015.02.017

Ehlmann, B. L., Mustard, J. F., Murchie, S. L., Bibring, J.-P., Meunier, A., Fraeman, A. a., & Langevin, Y. (2011). Subsurface water and clay mineral formation during the early history of Mars. *Nature*, *479*(7371), 53–60. https://doi.org/10.1038/nature10582

Evans, L. G., Reedy, R. C., Starr, R. D., Kerry, K. E., & Boynton, W. V. (2006). Analysis of gamma ray spectra measured by Mars Odyssey. *Journal of Geophysical Research*, *112*(E3), E03S04. https://doi.org/10.1029/2005JE002657

Feldman, W. C., Prettyman, T. H., Maurice, S., Plaut, J. J., Blish, D. L., Vaniman, D. T.,

et al. (2004). Global distribution of near-surface hydrogen on Mars. *Journal of Geophysical Research*, *109*(E9), E09006. https://doi.org/10.1029/2003JE002160

Fialips, C. I., Carey, J. W., Vaniman, D. T., Bish, D. L., Feldman, W. C., & Mellon, M. T. (2005). Hydration state of zeolites, clays, and hydrated salts under present-day martian surface conditions: Can hydrous minerals account for Mars Odyssey observations of near-equatorial water-equivalent hydrogen? *Icarus*, *178*(1), 74–83. https://doi.org/10.1016/j.icarus.2005.04.020

Goossens, S., Mazarico, E., Sabaka, T. J., Nicholas, J. B., Genova, A., & Neumann, G. A. (2017). Evidence for a low bulk crustal density for Mars from gravity and topography. *Geophysical Research Letters*, *44*(15), 7686–7694. https://doi.org/10.1002/2017gl074172

Grau Galofre, A., Bahia, R. S., Jellinek, A. M., Whipple, K. X., & Gallo, R. (2020). Did Martian valley networks substantially modify the landscape? *Earth and Planetary Science Letters*, *547*, 116482. https://doi.org/10.1016/j.epsl.2020.116482

Grott, M., & Wieczorek, M. A. (2012). Density and lithospheric structure at Tyrrhena Patera, Mars, from gravity and topography data. *Icarus*, *221*(1), 43–52. https://doi.org/10.1016/j.icarus.2012.07.008

Hamilton, V. E., Christensen, P. R., McSween, H. Y., & Bandfield, J. L. (2003). Searching for the source regions of martian meteorites using MGS TES: Integrating martian meteorites into the global distribution of igneous materials on Mars. *Meteoritics and Planetary Science*, *38*(6), 871–885. https://doi.org/10.1111/j.1945-5100.2003.tb00284.x

Hartmann, W. K., Neukum, G., Zentrum, D., & Berlin, D.-. (2001). CRATERING CHRONOLOGY AND THE EVOLUTION OF MARS 1 . Background : Cratering Studies and the Relation to Martian Rocks Through the process of impact cratering , Nature randomly stamps circular bowls of known shape on planetary surfaces . This fact offers us . *Nature*, (February), 165–194.

Hood, Don R., Karunatillake, S., Gasnault, O., Williams, A. J., Dutrow, B. L., Ojha, L., et al. (2019). Contrasting Regional Soil Alteration across the Topographic Dichotomy of Mars. *Geophysical Research Letters*, 1–10. https://doi.org/10.1029/2019GL084483

Hood, Donald R., Judice, T., Karunatillake, S., Rogers, D., Dohm, J. M., Susko, D. A., & Carnes, L. K. (2016). Assessing the geologic evolution of Greater Thaumasia, Mars. *Journal of Geophysical Research: Planets*, *121*(9), 1753–1769. https://doi.org/10.1002/2016JE005046

Karunatillake, S., Keller, J. M., Squyres, S. W., Boynton, W. V, Janes, D. M., Gasnault, O., & Newsom, H. E. (2007). Chemical compositions at Mars landing sites subject to Mars Odyssey Gamma Ray Spectrometer constraints. *Journal of Geophysical Research*, *112*, 1–16. https://doi.org/10.1029/2006JE002859

Karunatillake, S., Squyres, S. W., Gasnault, O., Keller, J. M., Janes, D. M., Boynton, W. V., & Finch, M. J. (2011). Recipes for Spatial Statistics with Global Datasets: A Martian Case Study. *Journal of Scientific Computing*, *46*(3), 439–451. https://doi.org/10.1007/s10915-010-9412-z

Kerber, L., & Head, J. W. (2010). The age of the Medusae Fossae Formation: Evidence of Hesperian emplacement from crater morphology, stratigraphy, and ancient lava contacts. *Icarus*, *206*(2), 669–684. https://doi.org/10.1016/j.icarus.2009.10.001

Kerber, L., Head, J. W., Madeleine, J.-B., Forget, F., & Wilson, L. (2012). The dispersal of pyroclasts from ancient explosive volcanoes on Mars: Implications for the friable layered deposits. *Icarus*, *219*(1), 358–381. https://doi.org/10.1016/j.icarus.2012.03.016

Mest, S., & Crown, D. (2014). Scientific Investigations Map 3245 Geologic Map of MTM – 30247 , – 35247 and – 40247 Quadrangles, Reull Vallis Region of Mars. *USGS Publication*. Retrieved from https://pubs.usgs.gov/sim/3245/pdf/sim3245_pamphlet.pdf

Michalski, J. R., Dobrea, E. Z. N., Niles, P. B., & Cuadros, J. (2017). Ancient hydrothermal seafloor deposits in Eridania basin on Mars. *Nature Communications*, *8*(May), 15978. https://doi.org/10.1038/ncomms15978

Moore, J. M., & Edgett, K. S. (1993). Hellas Planitia, Mars: Site of Net Dust Erosion and Implications for the Nature of Basin Floor Deposits, *20*(15), 1599–1602.

Mustard, J. F., Ehlmann, B. L., Murchie, S. L., Poulet, F., Mangold, N., Head, J. W., et al. (2009). Composition, morphology, and stratigraphy of Noachian crust around the Isidis basin. *Journal of Geophysical Research E: Planets*, *114*(12), 1–18. https://doi.org/10.1029/2009JE003349

Newsom, H. E., Crumpler, L. S., Reedy, R. C., Petersen, M. T., Newsom, G. C., Evans, L. G., et al. (2007). Geochemistry of Martian soil and bedrock in mantled and less mantled terrains with gamma ray data from Mars Odyssey. *Journal of Geophysical Research*, *112*, E03S12. https://doi.org/10.1029/2006JE002680

Ojha, L., & Lewis, K. (2018). The Density of the Medusae Fossae Formation: Implications for its Composition, Origin, and Importance in Martian History. *Journal of Geophysical Research: Planets*, *123*(6), 1368–1379. https://doi.org/10.1029/2018JE005565

Ojha, L., Lewis, K., Karunatillake, S., & Schmidt, M. (2018). The Medusae Fossae Formation as the single largest source of dust on Mars. *Nature Communications*, *9*(1), 1–7. https://doi.org/10.1038/s41467-018-05291-5

Ojha, L., Karunatillake, S., & Lacovino, K. (2019). Atmospheric Injection of Sulfur from the Medusae Fossae Forming Events. *Planetary and Space Science*, *179*, 104734. https://doi.org/10.1016/j.pss.2019.104734

Parro, L. M., Jiménez-Díaz, A., Mansilla, F., & Ruiz, J. (2017). Present-day heat flow model of Mars. *Scientific Reports*, *7*(April 2017), 45629. https://doi.org/10.1038/srep45629

Ruff, S. W., & Christensen, P. R. (2002). Bright and dark regions on Mars: Particle size and mineralogical characteristics based on Thermal Emission Spectrometer data. *Journal of Geophysical Research*, *107*(E12), 5127. https://doi.org/10.1029/2001JE001580

Salese, F., Ansan, V., Mangold, N., Carter, J., Ody, A., Poulet, F., & Ori, G. G. (2016). A sedimentary origin for intercrater plains north of the Hellas basin: Implications for climate conditions and erosion rates on early Mars. *Journal of Geophysical Research: Planets*, *121*(11), 2239–2267. https://doi.org/10.1002/2016JE005039

Smith, D. E., Head, J. W., Muhleman, D. O., Pettengill, G. H., Phillips, R. J., Solomon, S. C., et al. (2001). Mars orbiter laser altimeter: Experiment summary after the first year of global mapping of Mars. *Journal of Geophysical Research E: Planets*, *106*(10), 23689–23722.

Susko, D. A., Karunatillake, S., Kodikara, G., Skok, J. R., Wray, J., Heldmann, J., et al. (2017). A record of igneous evolution in Elysium, a major martian volcanic province. *Scientific Reports*, *7*, 43177. https://doi.org/10.1038/srep43177

Tanaka, K.L., Robbins, S. J., Fortezzo, C. M., Skinner, J. A., & Hare, T. M. (2014). The digital global geologic map of Mars: Chronostratigraphic ages, topographic and crater morphologic characteristics, and updated resurfacing history. *Planetary and Space Science*, *95*, 11–24. https://doi.org/10.1016/j.pss.2013.03.006

Tanaka, Kenneth L. (2002). Catastrophic erosion of Hellas basin rim on Mars induced by magmatic intrusion into volatile-rich rocks. *Geophysical Research Letters*, *29*(8), 1–4. https://doi.org/10.1029/2001GL013885

Taylor, G. J., Stopar, J. D., Boynton, W. V., Karunatillake, S., Keller, J. M., Brückner, J., et al. (2006). Variations in K/Th on Mars. *Journal of Geophysical Research*, *112*(E3), E03S06. https://doi.org/10.1029/2006JE002676

Taylor, G. J., Martel, L. M. V., Karunatillake, S., Gasnault, O., & Boynton, W. V. (2010). Mapping Mars geochemically. *Geology*, *38*(2), 183–186. https://doi.org/10.1130/G30470.1

Werner, S. C., & Tanaka, K. L. (2011). Redefinition of the crater-density and absolute-age boundaries for the chronostratigraphic system of Mars. *Icarus*, *215*(2), 603–607. https://doi.org/10.1016/j.icarus.2011.07.024

Wieczorek, M. A. (2015). *Gravity and Topography of the Terrestrial Planets*. *Treatise on Geophysics: Second Edition* (Vol. 10). Elsevier B.V. https://doi.org/10.1016/B978-0-444-53802-4.00169-X

Wieczorek, Mark A. (2008). Constraints on the composition of the martian south polar cap from gravity and topography. *Icarus*, *196*(2), 506–517. https://doi.org/10.1016/j.icarus.2007.10.026

Wieczorek, Mark A., & Simons, F. J. (2005). Localized spectral analysis on the sphere. *Geophysical Journal International*, *162*(3), 655–675. https://doi.org/10.1111/j.1365-246X.2005.02687.x

Wieczorek, Mark A., & Simons, F. J. (2007). Minimum-variance multitaper spectral estimation on the sphere. *Journal of Fourier Analysis and Applications*, *13*(6), 665–692. https://doi.org/10.1007/s00041-006-6904-1

Wilson, L., & Head, J. W. (2007). Explosive volcanic eruptions on Mars: Tephra and accretionary lapilli formation, dispersal and recognition in the geologic record. *Journal of Volcanology and Geothermal Research*, *163*(1–4), 83–97. https://doi.org/10.1016/j.jvolgeores.2007.03.007

Zalewska, N. (2013). Hellas Planitia as a potential site of sedimentary minerals. *Planetary and Space Science*, *78*, 25–32. https://doi.org/10.1016/j.pss.2012.12.006